Letter

Programmable and reconfigurable photonic simulator for classical *XY* models

Jiayi Ouyang, Yuxuan Liao, Xue Feng,* Yongzhuo Li, Kaiyu Cui, Fang Liu, Hao Sun, Wei Zhang, and Yidong Huang

Department of Electronic Engineering, Tsinghua University, Beijing 100084, China

(Received 16 April 2024; revised 31 May 2024; accepted 12 July 2024; published 1 August 2024)

In this work, we proposed and experimentally demonstrated a photonic simulator for *XY* models, which is a typical kind of classical spin model. By encoding the *XY* spins on the phase term of the input light field, the corresponding *XY* Hamiltonian could be performed on the output light intensities. The simulator is mainly based on a programmable and reconfigurable optical vector-matrix multiplication system, which can map arbitrary *XY* models within the dimensionality limit. Here, we demonstrated the Berezinskii-Kosterlitz-Thouless transition in a two-dimensional *XY* model, in which the values of some observables are calculated and consistent with the theory. Besides, we performed the ground-state search of two 25-spin *XY* models with different spin connections and coupling strengths. Our proposal paves the way to investigate the *XY* spin system.

DOI: 10.1103/PhysRevApplied.22.L021001

Simulating the dynamics of classical spin models is an issue in both physics and computer science [1]. The classical spin model consists of spins arranged in a lattice, in which the spin at site i is denoted with a unit-length vector $\mathbf{S}_i$. Given the spin-interaction matrix $\mathbf{J} = (J_{ij})$, the Hamiltonian of the spin system is $H = -\sum_{(i,j)} J_{ij}\mathbf{S}_i \cdot \mathbf{S}_j$. If the spins are planar rotors with $\mathbf{S}_i = (\cos\theta_i, \sin\theta_i)$, such models are known as *XY* models [2]. The *XY* model can be employed in directional statistics [3], or associated with some physical phenomena, including broken-symmetry transitions [2,4], superfluid thin films [5], superconductors [6], etc. Besides, searching the ground state of the *XY* model can be related to finding the optimal solution of the continuous complex constant modulus quadratic optimization problem, which is generally NP-hard and computationally intractable [2,7,8]. Recently, some physical platforms have been proposed to simulate *XY* models, including those based on optical parametric oscillators (OPOs) [3], polaritons [2,8,9], laser networks [7], and on-chip optical phased arrays [10]. However, it is still challenging to implement arbitrary interactions among *XY* spins. For instance, the spin modulation is time multiplexed and the couplings are introduced with the optical delay line in the *XY* simulator based on OPOs [3], in which implementing the all-to-all spin connections is difficult. In polariton simulators [2,8,9], the spin interactions mainly depend on the separation distances among the polaritons. For the laser-network approach, the aperture and lens are employed to achieve the weak and strong spin couplings, respectively [7]. Thus, it is hard for the polariton simulators and the laser networks to perform an *XY* model with arbitrary interactions. Additionally, in the on-chip optical phased array [10], the amount of tunable microring resonators cannot support the ability to map arbitrary *XY* models. As shown by the simulators mentioned above, there is still no programmable *XY* simulator that can perform arbitrary *XY* models and various tasks. In this work, we experimentally implemented a programmable and reconfigurable photonic simulator to demonstrate *XY* models with arbitrary coupling strengths and connections, which is an extension of our previously proposed phase-encoding and intensity-detection Ising annealer (PEIDIA) [11]. In the photonic simulator, *XY* spins are encoded on the phase term of the light field, which is similar to the spatial photonic Ising machines [11–13]. However, the method of mapping spin interactions is adjusted from the PEIDIA [11] to be suitable for *XY* models. Our proposed simulator is based on the optical vector-matrix multiplication (OVMM) platform and electronic feedback with heuristic algorithms. In each iteration, the light field encoding the spins is transformed by the OVMM, and then a photodetector measures the intensity. An electronic processor is utilized to compute the Hamiltonian from the optical intensity. Subsequently, it generates and updates the next spin configuration according to the employed heuristic algorithm for the next iteration. The OVMM is based on the beam-splitting and recombining architecture [11,14,15], which can perform arbitrary complex matrix transformations. Meanwhile, different algorithms can be flexibly applied in the electronic processor, thus various tasks can be performed with our proposed programmable

*Contact author: x-feng@tsinghua.edu.cn

and reconfigurable photonic simulator. In the experiments, we observed the phenomena of the Berezinskii-Kosterlitz-Thouless (BKT) transition [16] in the two-dimensional (2D) *XY* model with 400 spins. Besides, the ground-state search of two 25-spin *XY* models with different spin connections and coupling strengths was presented. Our method would provide a flexible and fast photonic system to simulate classical *XY* models.

Figure 1(a) shows a 2D *XY* model, where the spins are arranged in a square lattice. The spin at site $\mathbf{r}_i$, which is the translation vector of the spin i, possesses the azimuth angle $\theta_i \in [0, 2\pi)$ relative to the unit vector $\hat{\mathbf{x}}$, and can be denoted by the magnetization vector $\mathbf{S}_i = (\cos\theta_i, \sin\theta_i)$. The corresponding Hamiltonian can be obtained by summing all spin interactions [2,17]:

$$H = -\sum_{(i,j)} J_{ij}\,\mathbf{S}_i \cdot \mathbf{S}_j = -\frac{1}{2}\mathbf{\Theta}^{\mathrm{H}}\mathbf{J}\mathbf{\Theta}, \tag{1}$$

where (i,j) denotes a pair of spins at site $\mathbf{r}_i$ and $\mathbf{r}_j$ with interaction strength J_{ij}, and the superscript H denotes the conjugate transpose. Equation (1) indicates that the Hamiltonian can also be expressed with the complex quadratic form with the spin configuration vector $\mathbf{\Theta} = [\exp(\mathrm{i}\theta_1), \exp(\mathrm{i}\theta_2), \ldots]^{\mathrm{T}}$ (the superscript T denotes the transpose). To simulate such models, a photonic system is employed to encode the spin configuration on the light field and perform the spin interactions. As shown in Fig. 1(b), our proposed photonic *XY* simulator consists of three modules. The first is the beam-generation module that comprises a laser, a collimator, and a spatial light modulator (SLM). The SLM [SLM0 in Fig. 1(b)] splits the beam from the collimator into M beams, each of which will encode a spin. The second is the OVMM module with two SLMs [SLM1 and SLM2 in Fig. 1(b)], a pinhole, and a lens. SLM1 appends the phase delay θ_i to beam i, thus the input vector $\mathbf{\Theta}$ is encoded on the complex amplitude of the light field. Besides, SLM1 and SLM2 conduct the matrix transformation $\mathbf{A}$ by properly splitting and recombining the beams [11]. Then the pinhole filters out the beams with unwanted directions, and a lens aligns the beams to the optical axis. The last is the detection module, where a detector measures the optical intensities of the OVMM, $\mathbf{I} = (\mathbf{A\Theta})^{\mathrm{H}} \odot (\mathbf{A\Theta})$ ($\odot$ denotes the element-wise production). The detailed setup is provided within the Supplemental Material [18] (see also Refs. [11,15,17,19–21] therein). We noticed that the Hamiltonian in Eq. (1) can be directly calculated from $\mathbf{I}$ by configuring the transformation matrix $\mathbf{A}$ satisfying $\mathbf{A}^{\mathrm{H}}\mathbf{A} = \mathbf{J} + \mathbf{J}_D$ [18]:

$$H(\mathbf{\Theta}) = -\frac{1}{2}(\mathbf{A\Theta})^{\mathrm{H}}(\mathbf{A\Theta}) + H_0 = -\frac{1}{2}\sum_i I_i + H_0, \tag{2}$$

where $\mathbf{J}_D$ is a diagonal matrix, and H_0 is a constant. As our primary concern is the relative Hamiltonian, the constant term H_0 is neglected in the following discussion.

In the operation process of the simulator, the OVMM module is first configured according to the transformation matrix $\mathbf{A}$, which is unchanged during the following process. A spin state $\mathbf{\Theta}$ is generated and encoded as the input vector. Then an electronic processor is employed to calculate the Hamiltonian from the output intensities with Eq. (2), and decide whether to accept the current spin state or not. The above procedure from generating a spin state to the acceptance of such a state is regarded as one sampling. The sampling should be conducted iteratively to collect enough statistics according to the specific objectives.

Due to the full programmability of the OVMM, our simulator can demonstrate *XY* models with arbitrary connections and coupling strengths. Besides, the reconfigurability of our simulator allows us to configure different *XY* models and employ appropriate algorithms to carry out various tasks. In the experiment, two tasks including observing the phase transition and searching the ground states are demonstrated with different *XY* models.

First, our proposed photonic simulator is employed to demonstrate the BKT transition [16] by performing Boltzmann sampling of a 2D *XY* model under a series of temperature stages. The model has $N = 400$ spins in a square lattice ($L = 20$) with periodic boundary conditions. In this model, each spin interacts only with four nearest neighbors with the strength of $J_{ij} = 1$, as shown in Fig. 1(a). The Metropolis algorithm [22,23] is employed for the Boltzmann sampling. In each sampling iteration, the angle of one random spin is changed to a random direction.

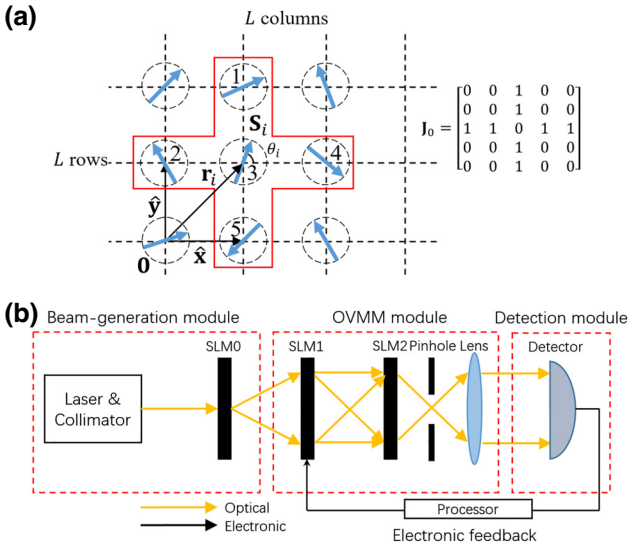

FIG. 1. Principle of the photonic simulator. (a) A two-dimensional *XY* model. (b) Experimental setup of the photonic simulator. The detailed principle of the OVMM is provided within the Supplemental Material [18]. Laser: ORION 1550-nm Laser Module. SLM: Holoeye PLUTO-2.1-TELCO-013. Detector: Hamamatsu InGaAs Camera C12741-03.

Then the spin perturbation is accepted with the probability of $\min[1, \exp(-\Delta H/T)]$, where ΔH is the Hamiltonian variation resulting from the perturbation. The annealing temperature T is the product of the Boltzmann constant and the real temperature for convenience. As the perturbation of a single spin involves $C = 5$ spins within the red box in Fig. 1(a), only the five spins, rather than the entire spins, are configured to the photonic simulator to calculate the Hamiltonian variation. Besides, the transformation matrix of the OVMM should be configured according to the five-spin interaction matrix $\mathbf{J}_0$ shown in Fig. 1(a). Since each site in the lattice is equivalent due to the periodic boundary condition, $\mathbf{J}_0$ and $\mathbf{A}$ are unchanged in the iterative sampling process. The maximum dimensionality of the employed OVMM is $M = 25$, hence our simulator can process $P = M/C = 5$ spin perturbations simultaneously. In each sampling iteration, P nonadjacent spins are randomly selected. Each selected spin combined with its neighbors forms a spin group including $C = 5$ spins. Then P spin groups are configured to the simulator, and the interaction energy $H_i^{(1)} (i = 1, 2, \ldots, P)$ of each group is calculated from the output intensities with Eq. (2). Then the P selected spins are perturbed, and the interaction energy $H_i^{(2)}$ $(i = 1, 2, \ldots, P)$ of each group is obtained. Each spin perturbation is accepted with the probability of $\min\{1, \exp[-(H_i^{(2)} - H_i^{(1)})/T]\}$. The accepted spin configurations are recorded for the following calculations.

The employed SLM has 8-bit grayscale so that the spins can only take angles of $2\pi n_i/q$ $(n_i = 0, 1, \ldots, q-1, q = 256)$. Additionally, considering the sampling speed of the SLM and the camera, $q = 32$ is chosen for demonstrating the BKT transition [24]. The annealing temperature T is slowly decreased from 2 to 0.2, including 19 stages with an interval of about 0.1. Each temperature stage has 2×10^4 sampling iterations, including 10^5 spin perturbations. The last 5×10^3 samplings in each temperature stage are used to calculate three observables under the corresponding temperature, including the magnetic susceptibility $\chi = \langle[\sum_i \cos(\theta_i)]^2\rangle/N$ [25], the spin-correlation function $G(r) = \langle S(\mathbf{r})S(\mathbf{0})\rangle$ [16], and the helicity modulus [4,26]

$$\Upsilon = -\frac{\langle H\rangle}{2N^2} - \frac{1}{TN^2}\left\langle\left[\sum_{(i,j)} \sin\left(\theta_i - \theta_j\right)\hat{\mathbf{e}}_{ij}\cdot\hat{\mathbf{x}}\right]^2\right\rangle, \quad (3)$$

where $\langle\cdot\rangle$ represents the average value under a certain temperature, $\hat{\mathbf{e}}_{ij} = (\mathbf{r}_j - \mathbf{r}_i)/|\mathbf{r}_j - \mathbf{r}_i|$ is the unit translation vector from site i to j, $\hat{\mathbf{x}}$ is the unit vector of x axis in the lattice plane as shown in Fig. 1(a), and the sum is over the nearest-neighbor lattice sites. Figure 2(a) shows the evolution of the magnetic susceptibility χ. It can be observed that when temperature $T > 1.2$, χ fluctuates only within a small range around the mean value

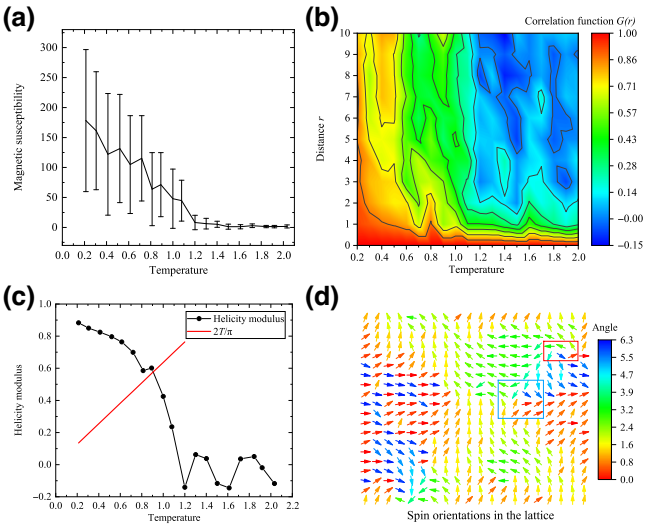

FIG. 2. The measured experimental observables of the 2D XY model. (a) The magnetic susceptibility vs the temperature. The error bar shows the standard deviation. (b) The correlation function vs distance and temperature. (c) The helicity modulus versus the temperature. The straight curve is $2T/\pi$ and the intersection of the two curves denotes the critical point. (d) Observation of a bound vortex-antivortex pair below the critical temperature. The red box and the blue box denote a vortex and an antivortex, respectively.

close to 0, which indicates that the spin system is highly disordered. When T decreases under the value of 1.2, the mean value of χ rapidly grows and χ distributes within a broader range, which indicates the ferromagnetism of the system. The spin correlation function denotes the correlation between the spin directions at position $\mathbf{r}$ and position $\mathbf{0}$ as shown in Fig. 1(a). The values of $G(r)$ $(r = |\mathbf{r}|)$ under different temperatures are illustrated in Fig. 2(b). It can be seen that $G(r)$ decays sharply when $T > 1.2$, indicating that the spin directions are highly uncorrelated. When $0.6 < T < 1.2$, the decay of $G(r)$ is slower. Suddenly, $G(r)$ decays very slowly when $T < 0.6$, which shows a quasi-long-range order. Such results are consistent with the theoretical predictions [16]. Thus, the system experienced a BKT transition: when T is higher than the critical temperature T_c, $G(r)$ experiences a power-law decay, while $G(r)$ decays exponentially when $T < T_c$. To obtain the accurate critical temperature T_c, the evolution of the helicity modulus Υ is shown in Fig. 2(c). Figure 2(c) shows that Υ fluctuates around 0 when T decreases from 2 to 1.2, while Υ increases rapidly when T further decreases to 0.2. The intersection of the measured curve and the line of $2T/\pi$ denotes the critical temperature $T_c \approx 0.91$ [4]. Besides, another evidence corresponding to the topological characteristic in the BKT transition is the vortices and antivortices [16]. To simulate such a phenomenon, another sampling is conducted at the temperature of around 0.1, which is much below T_c. After about 6000 iterations,

the recorded spin orientations are shown in Fig. 2(d). It can be observed that there is a vortex (the red box) and an antivortex (the blue box), which is consistent with the theory [16].

Besides the sparse model, different XY models with arbitrary connections and coupling strength can also be demonstrated with our proposed simulator. The ground-state search of two 25-spin XY models is performed experimentally. Here, the SLMs perform the maximum spin angle levels of $q = 256$, which is high enough to approximate an XY model. When solving XY models mapped from optimization problems rather than real spin systems, the connections and coupling strengths would be complicated, hence two models are randomly generated as follows. For model 1, the spin-coupling strengths are uniformly distributed in $[-1, 1]$, and the graph density $2Q/[M(M-1)]$, (Q is the number of the spin connections and M is the number of spins) is 0.56 as shown in the inset of Fig. 3(a). Model 2 is fully connected with coupling strengths uniformly distributed in $\{-1, 1\}$ and is also shown in the inset of Fig. 3(a). The interaction matrices of models 1 and 2 are provided within the Supplemental Material [18]. When dealing with XY models with complicated interactions, all 25 spins have to be implemented in the simulator simultaneously. According to Eq. (1), finding the ground state can be regarded as solving an NP-hard continuous complex quadratic optimization problem [2,17]. Here, heuristic algorithms are employed to obtain the near-optimal solutions efficiently [27], and our adopted algorithm is based on fast simulated annealing [20,21]. In each iteration, a 25-dimensional Cauchy variable $\Delta\mathbf{\Theta}$ is added to the current spin configuration $\mathbf{\Theta}$. The spin configuration $\mathbf{\Theta} + \Delta\mathbf{\Theta}$ is accepted with probability of $\min[1, \exp\{-[H(\mathbf{\Theta} + \Delta\mathbf{\Theta}) - H(\mathbf{\Theta})]/T\}]$. The temperature T is gradually decreased and the near-optimal solutions are obtained finally. The experimental results are shown in Fig. 3. Then, 50 runs of the ground-state search are conducted for each model. For clarity, only one of the 50 experimental Hamiltonian evolution curves of models 1 and 2 is shown in Fig. 3(a) (all curves are provided within the Supplemental Material [18]). The red and yellow regions in Fig. 3(a) denote the distribution regions of the measured experimental Hamiltonian in each iteration of models 1 and 2, respectively. It can be seen that the curve quickly converges to a low Hamiltonian within about 1000 iterations for model 1 and 1500 iterations for model 2. To evaluate the searching performance, we consider one search to be successful when the final accepted Hamiltonian is lower than the lowest Hamiltonian (obtained in the simulation, $H_{\min} \approx -77.0$ for model 1 and -193.8 for model 2) multiplied by a tolerance coefficient η since it is hard to find the exact global optimum. The experimental final successful probabilities of models 1 and 2 under different tolerance coefficients are shown in Fig. 3(b). The final successful probabilities are close to 1 when $\eta < 0.9$, but rapidly decrease to 0 when η increases to 0.98. For comparison, numerical simulation results are also shown in Fig. 3(b), and the successful probabilities for both models are 1 with $\eta = 0.96$. Such deteriorations in the experiment result from the noise induced by the experimental system, even though the average fidelities of all effective samplings are as high as 0.9970 ± 0.0033 and 0.9967 ± 0.0031 for models 1 and 2, respectively. The noise level can be estimated with the relative deviation of the experimental Hamiltonian near the ground state, which is $R_1 = 2.67\%$ for model 1 and $R_2 = 2.62\%$ for model 2. The photonic simulator cannot distinguish two states when their relative Hamiltonian variation is less than the noise level. Figure 3(b) shows that the experimental successful probability first decreases to 0 when $\eta \approx 1 - R$ for models 1 and 2, which indicates that our noise estimation is reasonable. The detailed noise analysis is provided within the Supplemental Material [18]. Nevertheless, the experimental results validate the capability of our photonic simulator to solve XY models with complicated connections and interactions.

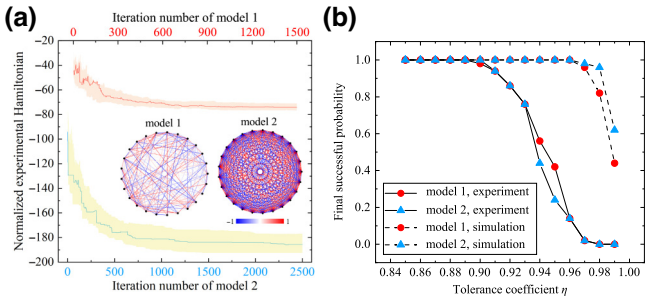

FIG. 3. Results of the ground-state search of the randomly generated XY models. (a) The red and yellow regions denote the distribution intervals of 50 normalized experimental Hamiltonian evolution curves of models 1 and 2, respectively. The red or blue curve shows one of the 50 curves, respectively. The insets show the corresponding models, where the black dots denote the XY spins and the interaction strengths are referred from the colorbar. (b) The final successful probabilities vs the tolerance coefficient. The results of both the experiment and simulation are shown.

In this article, we proposed a programmable and reconfigurable photonic XY simulator, which can demonstrate XY models with arbitrary interactions and various tasks. After encoding the spin configuration on the phase term of the light field, our simulator can provide the corresponding Hamiltonian within the propagation time of light beam. To validate our proposal, we demonstrate the BKT transition of the 2D XY model and perform the ground-state search of two models with different connections and coupling strengths.

Two major issues can be further improved for our proposal. The first is to increase the dimensionality of the OVMM, which is helpful to process more spin perturbations simultaneously in sparse models, or deal

with complex models with higher dimensionalities. In our employed OVMM, increasing the dimensionality could be achieved by reducing the size of the Gaussian beam (constrained by paraxial approximation) and employing SLMs with larger areas. Besides, other optical computation schemes could also be utilized to implement our photonic simulator, such as the on-chip Mach-Zehnder interferometer arrays [28,29].

The second is the time consumption of the optoelectronic conversion in the SLMs and camera, which limits the computation speed of our simulator. In the future, the utilization of the high-speed phase modulators [30] and detectors [31] would improve the state-sampling speed in the optical domain. In the electronic domain, the speed can be increased by employing an FPGA, or analog computing devices [32].

Acknowledgments. This work was supported by the National Key Research and Development Program of China (Grants No. 2018YFB2200402, No. 2017YFA030 3700), and the National Natural Science Foundation of China (Grant No. 61875101). This work was also supported by Beijing academy of quantum information sciences, Beijing National Research Center for Information Science and Technology (BNRist), Frontier Science Center for Quantum Information, and Tsinghua Initiative Scientific Research Program.

[1] R. S. Zemel, C. K. Williams, and M. C. Mozer, Lending direction to neural networks, Neural Netw. **8**, 503 (1995).
[2] N. G. Berloff, M. Silva, K. Kalinin, A. Askitopoulos, J. D. Töpfer, P. Cilibrizzi, W. Langbein, and P. G. Lagoudakis, Realizing the classical *XY* Hamiltonian in polariton simulators, Nat. Mater. **16**, 1120 (2017).
[3] Y. Takeda, S. Tamate, Y. Yamamoto, H. Takesue, T. Inagaki, and S. Utsunomiya, Boltzmann sampling for an *XY* model using a non-degenerate optical parametric oscillator network, Quantum Sci. Technol. **3**, 014004 (2017).
[4] H. Weber and P. Minnhagen, Monte Carlo determination of the critical temperature for the two-dimensional *XY* model, Phys. Rev. B **37**, 5986 (1988).
[5] P. H. Nguyen and M. Boninsegni, Superfluid transition and specific heat of the 2D *x*-*y* model: Monte Carlo simulation, Appl. Sci. **11**, 4931 (2021).
[6] L. Benfatto, A. Toschi, and S. Caprara, Low-energy phase-only action in a superconductor: A comparison with the XY model, Phys. Rev. B **69**, 184510 (2004).
[7] I. Gershenzon, G. Arwas, S. Gadasi, C. Tradonsky, A. Friesem, O. Raz, and N. Davidson, Exact mapping between a laser network loss rate and the classical XY hamiltonian by laser loss control, Nanophotonics **9**, 4117 (2020).
[8] K. P. Kalinin, A. Amo, J. Bloch, and N. G. Berloff, Polaritonic XY-Ising machine, Nanophotonics **9**, 4127 (2020).
[9] P. G. Lagoudakis and N. G. Berloff, A polariton graph simulator, New J. Phys. **19**, 125008 (2017).
[10] M. Chalupnik, A. Singh, J. Leatham, M. Lončar, and M. Soltani, in *Frontiers in Optics + Laser Science 2022 (FIO, LS)* (Optica Publishing Group, Rochester, New York, United States, 2022), p. JTu7B.6.
[11] J. Ouyang, Y. Liao, Z. Ma, D. Kong, X. Feng, X. Zhang, X. Dong, K. Cui, F. Liu, W. Zhang, and Y. Huang, On-demand photonic Ising machine with simplified Hamiltonian calculation by phase encoding and intensity detection, Commun. Phys. **7**, 168 (2024).
[12] D. Pierangeli, G. Marcucci, and C. Conti, Large-scale photonic Ising machine by spatial light modulation, Phys. Rev. Lett. **122**, 213902 (2019).
[13] Y. Fang, J. Huang, and Z. Ruan, Experimental observation of phase transitions in spatial photonic Ising machine, Phys. Rev. Lett. **127**, 043902 (2021).
[14] P. Zhao, S. Li, X. Feng, S. M. Barnett, W. Zhang, K. Cui, F. Liu, and Y. Huang, Universal linear optical operations on discrete phase-coherent spatial modes with a fixed and non-cascaded setup, J. Opt. **21**, 104003 (2019).
[15] S. Li, S. Zhang, X. Feng, S. M. Barnett, W. Zhang, K. Cui, F. Liu, and Y. Huang, Programmable coherent linear quantum operations with high-dimensional optical spatial modes, Phys. Rev. Appl. **14**, 024027 (2020).
[16] V. N. Ryzhov, E. E. Tareyeva, Y. D. Fomin, and E. N. Tsiok, Berezinskii–Kosterlitz–Thouless transition and two-dimensional melting, Phys.-Usp. **60**, 857 (2017).
[17] A. M.-C. So, J. Zhang, and Y. Ye, On approximating complex quadratic optimization problems via semidefinite programming relaxations, Math. Program. **110**, 93 (2007).
[18] See Supplemental Material at http://link.aps.org/supplemental/10.1103/PhysRevApplied.22.L021001 for more details on the methods, experiment, and fidelity analysis, which includes Refs. [11,15,17,19–21].
[19] C. Roques-Carmes, Y. Shen, C. Zanoci, M. Prabhu, F. Atieh, L. Jing, T. Dubček, C. Mao, M. R. Johnson, V. Čeperić, J. D. Joannopoulos, D. Englund, and M. Soljačić, Heuristic recurrent algorithms for photonic Ising machines, Nat. Commun. **11**, 249 (2020).
[20] H. Szu and R. Hartley, Fast simulated annealing, Phys. Lett. A **122**, 157 (1987).
[21] L. Ingber and B. Rosen, Genetic algorithms and very fast simulated reannealing: A comparison, Math. Comput. Model. **16**, 87 (1992).
[22] S. Kirkpatrick, C. D. Gelatt, and M. P. Vecchi, Optimization by simulated annealing, Science **220**, 671 (1983).
[23] P. J. M. van Laarhoven and E. H. L. Aarts, in *Simulated Annealing: Theory and Applications*, edited by M. Hazewinkel, F. Calogero, Yu. I. Manin, A. H. G. Rinnooy Kan, and G.-C. Rota (Springer, Dordrecht, 1987), pp. 7–15.
[24] C. M. Lapilli, P. Pfeifer, and C. Wexler, Universality away from critical points in two-dimensional phase transitions, Phys. Rev. Lett. **96**, 140603 (2006).
[25] U. Wolff, Collective Monte Carlo updating for spin systems, Phys. Rev. Lett. **62**, 361 (1989).
[26] M. Hasenbusch, The two-dimensional XY model at the transition temperature: a high-precision Monte Carlo study, J. Phys. A **38**, 5869 (2005).
[27] J. Hromkovič, in *Algorithmics for Hard Problems: Introduction to Combinatorial Optimization, Randomization,*

Approximation, and Heuristics, edited by W. Brauer, G. Rozenberg, and A. Salomaa (Springer, Berlin, Heidelberg, New York, Hong Kong, London, Milan, Paris, Tokyo, 2003).

[28] J. Carolan, C. Harrold, C. Sparrow, E. Martín-López, N. J. Russell, J. W. Silverstone, P. J. Shadbolt, N. Matsuda, M. Oguma, M. Itoh, G. D. Marshall, M. G. Thompson, J. C. F. Matthews, T. Hashimoto, J. L. O'Brien, and A. Laing, Universal linear optics, Science **349**, 711 (2015).

[29] Y. Shen, N. C. Harris, S. Skirlo, M. Prabhu, T. Baehr-Jones, M. Hochberg, X. Sun, S. Zhao, H. Larochelle, D. Englund, and M. Soljačić, Deep learning with coherent nanophotonic circuits, Nat. Photonics **11**, 441 (2017).

[30] D. Renaud, D. R. Assumpcao, G. Joe, A. Shams-Ansari, D. Zhu, Y. Hu, N. Sinclair, and M. Loncar, Sub-1 volt and high-bandwidth visible to near-infrared electro-optic modulators, Nat. Commun. **14**, 1496 (2023).

[31] L. Vivien, A. Polzer, D. Marris-Morini, J. Osmond, J. M. Hartmann, P. Crozat, E. Cassan, C. Kopp, H. Zimmermann, and J. M. Fédéli, Zero-bias 40 Gbit/s germanium waveguide photodetector on silicon, Opt. Express **20**, 1096 (2012).

[32] Y. Chen, M. Nazhamaiti, H. Xu, Y. Meng, T. Zhou, G. Li, J. Fan, Q. Wei, J. Wu, F. Qiao, L. Fang, and Q. Dai, All-analog photoelectronic chip for high-speed vision tasks, Nature **623**, 48 (2023).